ELSEVIER

Journal of Fluids and Structures 23 (2007) 249–268

JOURNAL OF FLUIDS AND STRUCTURES

www.elsevier.com/locate/jfs

Features of flow-induced forces deduced from wavelet analysis

X.Q. Wang[a,*], R.M.C. So[a,b], W.-C. Xie[c]

[a]*Department of Mechanical Engineering, The Hong Kong Polytechnic University, Hung Hom, Kowloon, Hong Kong, PR China*
[b]*Industrial Center, The Hong Kong Polytechnic University, Hung Hom, Kowloon, Hong Kong, PR China*
[c]*Department of Civil Engineering, University of Waterloo, Waterloo, Ont., Canada*

Received 22 December 2005; accepted 11 September 2006
Available online 28 November 2006

Abstract

In the present study, the effect of Reynolds number (Re) on flow interference between two side-by-side stationary cylinders and the associated flow-induced forces are investigated using finite element method and wavelet analysis. The pitch ratio chosen is $T/D = 1.7$, where T is the separation distance measured between cylinder centers and D is the diameter, and Re, based on the free-stream velocity and the diameter of the cylinder, is varied within the laminar flow regime, i.e., $60 < \mathrm{Re} < 200$. The method of continuous wavelet transform is used to analyze time-variant features of flow-induced forces in the time–frequency domain. Flow patterns in the form of vorticity plots are presented to demonstrate the underlying physics. It is found that flow interference initially occurs in the inner vortices shed from the two cylinders, and extends to the outer vortices with increasing Re. The flow behind two cylinders undergoes three regimes: Regime I—unbiased gap flow, Regime II—stable biased gap flow, and Regime III—unstable gap flow. Flow-induced forces show significant variations when the flow transits from one regime to another. In particular, during the transition from Regimes II to III, the forces not only increase by amplitude, but also change their nature from deterministic to random, and show some nonstationary features. This is shown to be caused by the amalgamation of inner and outer vortices behind the two cylinders when the flow interference extends from inner vortices to outer vortices. Whenever possible, the present results are compared with experimental measurements and theoretical predictions. The numerical simulations are consistent with these other results.

Keywords: Two side-by-side cylinders; Flow-induced forces; Reynolds number effect; Wavelet analysis

1. Introduction

Two side-by-side cylinders in cross-flow is of common occurrence in various engineering applications, e.g., two chimneys in civil engineering, two struts in aeronautical engineering, and transmission lines in electrical engineering. It is also a representative case of cylinder arrays in cross-flow where structural instability is of major concern. Compared with one single cylinder in cross-flow, a distinctive feature of two cylinders in cross-flow is the interference between the two cylinders when they are in close proximity to each other. The interference could affect vortex shedding from the two cylinders and the associated flow-induced forces. The extent of the interference effect depends on many parameters, the more important of which is the pitch ratio, T/D, where T is the separation distance measured between cylinder centers

*Corresponding author. Tel.: +852 27664502; fax: +852 23654703.
E-mail address: mmxqwang@polyu.edu.hk (X.Q. Wang).

0889-9746/$ - see front matter © 2006 Elsevier Ltd. All rights reserved.
doi:10.1016/j.jfluidstructs.2006.09.002

and D the diameter. This flow interference behavior has been investigated by numerous researchers; recent reviews have been provided by Chen (1986), Wardlaw (1994), and Zdravkovich (2003).

In the case of two side-by-side stationary cylinders in cross-flow, the interference behavior can be classified according to T/D (Zdravkovich, 2003). For a finite range of Reynolds number (Re), two coupled vortex streets are observed in the first regime where T/D is moderate, i.e., $2.3<T/D<4$. They have the same shedding frequency but are coupled in out-of-phase mode. In the second regime, which covers the range $1.1<T/D<2.3$, a biased gap flow pattern appears. The third regime is characterized by two strongly coupled wakes which behave like the wake behind a single bluff body. The T/D in this regime is given by $T/D<1.1$. This classification still holds when the two cylinders are freely vibrating due to the excitation of flow-induced forces, except that the T/D values separating these regimes are slightly modified. While the interference behavior is relatively easy to understand for two side-by-side cylinders in the first and third regimes, the interference in the second regime remains a mystery, as stated by Zdravkovich (2003) who said "…the bi-stable biased gap flow has two paradoxical features. The first is that an entirely symmetrical oncoming flow leads to asymmetric narrow and wide wakes behind the two identical side-by-side cylinders. The second is that a uniform and stable flow induces a non-uniform and random bi-stable flow." The present study attempts to shed some light on the behavior of the biased gap flow pattern in the second regime and the role Re plays on this behavior.

Extensive studies have been carried out to investigate the biased gap flow. Bearman and Wadcock (1973) suggested that the biased gap flow is due to wake interactions through an experimental study. For the pitch ratio $1.1<T/D<2.3$ at $\mathrm{Re}=2.5\times10^4$, the flow was found to be bi-stable, intermittently changing over from one side to the other. The cylinder with a narrow wake has a lower base pressure and a higher mean drag coefficient. This was interpreted by Williamson (1985) as harmonic vortex-shedding modes associated with three Strouhal numbers (St's) around 0.1, 0.2, and 0.3, respectively, where the second harmonic mode (St around 0.2) is dominant. Kim and Durbin (1988) termed this phenomenon as a flopping phenomenon, which was found for $1.1<T/D<2$ at $\mathrm{Re}=2200$–6200, and it was noticed that the time duration of flopping follows a zero-event Poisson distribution. Sumner et al. (1997) used the technique of particle image velocimetry (PIV) to trace the vortex dynamics for impulsively started flow around two or three side-by-side cylinders. For two side-by-side cylinders with $1.5<T/D<3.0$, a strong gap flow was observed. This gap flow initiates breakup of the recirculation zones and vortex shedding. Near wakes of individual cylinders are asymmetric and biased towards the gap flow, while the far wake is marked by a single counter-rotating vortex pair.

For an oncoming steady cross-flow, however, Sumner et al. (1999) showed that the biased flow is associated with synchronized vortex shedding. Guillaume and LaRue (1999) measured the base pressure coefficient C_p at $\mathrm{Re}=4400$ for $T/D=1.75$, and the result showed a flopping phenomenon. From the power spectra of the measured flow velocities, it was found that a low St ($\mathrm{St}=0.11$) is associated with a wide wake while a high St ($\mathrm{St}=0.32$) is associated with a narrow wake. Furthermore, Guillaume and LaRue (2003) studied the variation of power spectra of the flow velocity during the flopping, showing that the dominant frequency in the wake changes between $\mathrm{St}=0.13$ and 0.29. Alam et al. (2003) found that, at $\mathrm{Re}=55000$, there exists an intermediate flow pattern in the flopping, where the direction of the gap flow is parallel to that of the free stream and the corresponding St is almost equal to that of a single cylinder, i.e., $\mathrm{St}=0.2$.

Numerical simulations have also been carried out to investigate the nature of the biased gap flow. Chang and Song (1990) used a finite element method (FEM)—boundary element method (BEM) combined approach to simulate the flow around two side-by-side cylinders for $T/D=1.7$ at $\mathrm{Re}=100$, showing that there is only one combined wake and the vortex shedding is asymmetric with the gap flow. The biased gap flow for two side-by-side cylinders at $T/D=1.5$ was reproduced at $\mathrm{Re}=200$ by Slaouti and Stansby (1992) and at $\mathrm{Re}=1000$ by Ichioka et al. (1997), which a discrete vortex method was used to simulate the flow past two side-by-side cylinders. Ng et al. (1997) showed that the flip-flopping behavior is due to the asymmetry of one of the gap vortices. In the simulation at $\mathrm{Re}=100$–200 for $T/D=1.5$–4.0, it was found difficult to identify isolated frequency peaks. Meneghini et al. (2001) showed that the Fourier spectra appear to be banded with a smooth peak around 0.2. Liu et al. (2001) found that the time histories of the flow-induced forces appear to be strongly irregular for $T/D=1.8$ at $\mathrm{Re}=200$ and the forces were suspected to be inherently nonstationary. The power spectrum of the lift force has two peaks centering at $\mathrm{St}=0.2$. A numerical simulation has been carried out by Chen et al. (2003) at $\mathrm{Re}=750$ for $T/D=1.7$, where large eddy simulation (LES) was used to simulate turbulent flow. A bi-stable biased flow was observed, which appeared to be the consequence of the use of a turbulence model. The wide wake gives $\mathrm{St}=0.16$, and the narrow wake yields $\mathrm{St}=0.24$. It should be noted that the authors showed that the spectrum of the flow velocity varies significantly with spatial position.

Two-dimensional flow around two stationary side-by-side cylinders was simulated at $\mathrm{Re}=1000$ for $T/D=1.5$ by Jester and Kallinderis (2003). It was found that the biased flow persists for 5–10 periods of vortex shedding, then

transitions to another biased flow. The wide wake has a dominant frequency St = 0.23, and the dominant frequency of the narrow wake occurs at St = 0.30. So and Wang (2003) used a FEM to simulate flow-induced vibration of two side-by-side cylinders in cross flows. The method of short-time Fourier transform was used to investigate nonstationary features of the flow-induced forces and the corresponding cylinder vibrations of two side-by-side elastic cylinders for $T/D = 1.7$ at Re = 800. It was shown that three different types of power spectrum exist, i.e. type A, a spectrum with a single dominant frequency occurring at St = 0.2, type B, a spectrum with two dominant frequencies occurring at St = 0.1 and 0.2 or St = 0.2 and 0.3, and type C, a spectrum with three dominant frequencies occurring at St = 0.1, 0.2, and 0.3. These three types of spectrum appear intermittently in a random way.

Despite a number of papers on this subject having been published, very few of them were concerned with the effect of Re. Peschard and Le Gal (1996) extended the Landau equation to this two-cylinder case, giving a physical interpretation of the behavior of wake interference. The model showed that the coupling between two cylinders is proportional to the reduced Re; hence increasing Re has the same effect as increasing T/D of the two cylinders. Three stationary flow regimes, that is, in-phase locking, phase-opposition locking, and asymmetric locking, were identified. These three regimes correspond to the regimes of single vortex street, biased flow, and coupled vortex streets as reported in the literature. However, the bi-stable biased flow was considered not an intrinsic feature of the wakes but due to upstream turbulent perturbations. Besides, an additional nonstationary regime was found, where the amplitude of the flow velocity and the phase difference between the two cylinders are oscillating in time. This is termed the quasiperiodic regime. For a given T/D, the wake may experience a successive variation through all or several of the aforementioned four states with an increment of Re. The effect of Re on the dominant frequencies of the flow velocity and the features of flow structure was investigated experimentally in the range of $T/D = 1.2$–1.6 (Xu et al, 2003), where Re varied from 150 to 14300. For a given T/D, one single vortex street was found at low Re, which is associated with one single dominant frequency in the flow velocity. When Re is increased, the wake transits to two asymmetric vortex streets associated with two dominant frequencies in the flow velocity. The transition was conjectured to be due to the fact that the gap flow breaks up a small closed wake (arising from the near-wall effect) when Re exceeds a critical value, leading to two (one narrow and one wide) asymmetric vortex streets in the wake.

In the study of flow-induced vibration of two cylinders, concern should not only be limited to the flow patterns, but should also be extended to the flow induced forces which are essential for the estimation of cylinder vibrations induced by the flow and their coupling with flow-induced forces. Understanding of this coupling between flow and vibrations is of importance to many branches of engineering, such as in the design of heat exchangers, nuclear reactors, and offshore drilling platforms. Furthermore, understanding of this interaction behavior could help the design of these engineering systems to avoid being operating too close to any instability boundary.

In the present study, flow-induced forces on two side-by-side stationary cylinders are calculated from numerical simulations using a FEM as developed by So and Wang (2003). The pitch ratio is selected at $T/D = 1.7$, a typical value for the biased-flow regime. In order to investigate the Re effect, focus is placed on the laminar regime, that is, $\mathrm{Re} < 200$, where Re is based on the free-stream velocity and the diameter of the cylinder, is considered. With this T/D and Re, the flow and the flow-induced forces might be random and nonstationary. Therefore, the method of continuous wavelet transform (CWT) is used to process the time series in order to investigate the nonstationary features of the flow-induced forces, thus allowing the true characteristics of the unsteady forces to be revealed.

2. Numerical approach

A finite element approach has been developed for the simulation of elastic beam vibration in a cross-flow (Wang et al., 2001; So and Wang, 2003). In the present study, this approach is used to solve the flow field around two side-by-side stationary cylinders; then the lift and drag forces acting on the cylinders are calculated for further analysis. A cross-flow of incompressible, viscous Newtonian fluid around two side-by-side stationary cylinders is considered. The upstream flow is assumed to be uniform and laminar with $\mathrm{Re} \leqslant 200$. The dimensionless Navier–Stokes equations are written as

$$\frac{\partial \mathbf{u}}{\partial t} + (\mathbf{u} \cdot \nabla)\mathbf{u} = -\nabla p + \frac{1}{\mathrm{Re}} \nabla^2 \mathbf{u}, \tag{1}$$

$$\nabla \cdot \mathbf{u} = 0, \tag{2}$$

where $\mathbf{u}$ is the dimensionless velocity vector normalized by the free-stream velocity U_∞, $t = t^* U_\infty / D$ the dimensionless time, p the dimensionless pressure normalized by ρU_∞^2, $\mathrm{Re} = U_\infty D / v$ the Re, D the diameter of the cylinder, p the fluid density, and v the kinematic viscosity of the fluid.

The boundary and initial conditions are given by

$$\mathbf{u}|_s = \begin{cases} U_\infty = 1 & \text{upstream far-field, top and bottom boundaries,} \\ \dfrac{\partial \mathbf{u}}{\partial n} = 0 & \text{downstream far-field} \end{cases} \tag{3a}$$

and

$$\mathbf{u}|_{t=0} = \begin{cases} 1 & \text{upstream far-field,} \\ 0 & \text{downstream far-field, top and bottom boundaries,} \end{cases} \tag{3b}$$

respectively, where the subscript S represents the boundary of the domain V occupied by the fluid. Far away from the cylinders (top and bottom boundaries), the flow is assumed to approach the undisturbed upstream velocity, $U_\infty = 1$. For the downstream far-field boundary, a parabolic condition is invoked, where n represents normal direction to the boundary.

An operator-splitting method (Glowinski and Pironneau, 1992) is used to solve the Navier–Stokes equation, and the software package *Fastflo* (Stokes and Mooney, 1994) is used to implement the method. The software package *Fastflo* is a general finite element package developed by CSIRO, Australia, for solving partial differential equations which govern physical processes in the fields of fluid mechanics, solid mechanics, electromagnetics, etc. Compared with commercial finite element packages, *Fastflo* is appropriate for research purpose since it is flexible in the specification of the governing equation and the solver. This is accomplished through the use of a high-level language, *Fasttalk*, associated with the package. It also allows the users to write or modify the codes for their individual models.

The computational domain along with the mesh used in the computation is shown in Fig. 1. The mesh has 99 503 nodes and 49 502 six-node triangular elements, with 64 points along the circumference of each cylinder. A test of grid dependence has been carried out where different meshes ranging from coarser to finer grids were used until the drag coefficient becomes mesh independent (So et al., 2001; Liu et al., 2001). The present mesh is more than sufficient to resolve the flow velocity field and the boundary layers around the cylinders.

Once the velocity and the pressure fields are obtained, the induced force on the structure is calculated using the following formula:

$$\mathbf{F}(t) = \oint \left(-p\mathbf{n} + \frac{1}{\mathrm{Re}} (\nabla \mathbf{u} + \nabla \mathbf{u}^{\mathrm{T}}) \cdot \mathbf{n} \right) \mathrm{d}c, \tag{4}$$

where the integration is performed around the circumference of the cylinder with arc length c, and $\mathbf{n}$ is the outward unit vector normal to the cylinder. The instantaneous force vector, $\mathbf{F} = \{F_x,\ F_y\}$ consists of two components: the

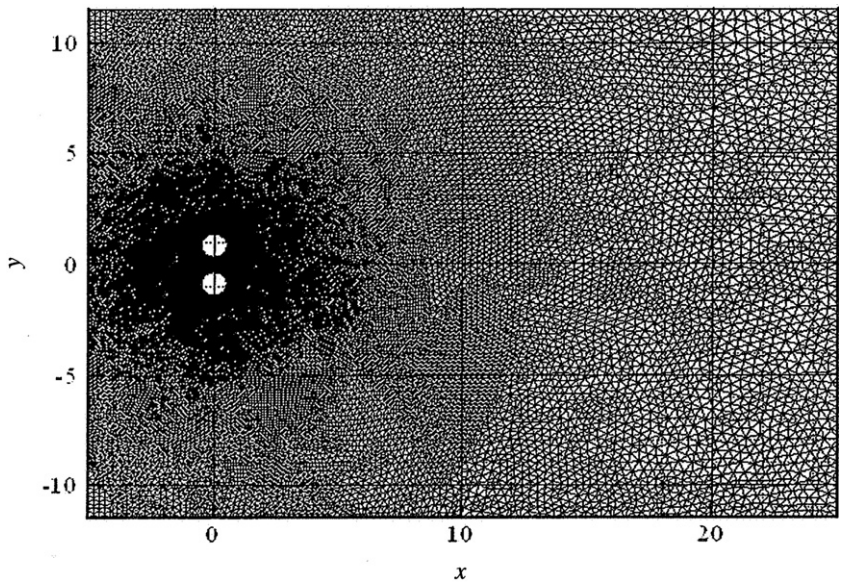

Fig. 1. Computational domain and the mesh used in the numerical simulation.

dimensionless unsteady drag and lift forces, respectively. Thus, the drag and lift force coefficients are defined as $c_D = 2F_x/(\rho U_\infty^2 D)$ and $c_L = 2F_y/(\rho U_\infty^2 D)$, respectively. All calculated results are presented in the form of time series. From this point on, an overbar denotes the mean value and primes are used to designate the root-mean-square (r.m.s.) value of the signal. For example, the mean and r.m.s. values of the instantaneous c_D are $\bar{C}_D$ and C'_D, respectively.

3. Continuous wavelet transform

CWT of the lift and drag coefficient is carried out to investigate their nonstationary character as a function of Re. The CWT is defined as

$$\mathrm{CWT}(s,\tau) = \frac{1}{\sqrt{s}} \int_{-\infty}^{\infty} w(t)\psi^*\left(\frac{t-\tau}{s}\right) \mathrm{d}t, \tag{5}$$

where $w(t)$ is the data to be analyzed, $\psi(t)$ is called, the mother wavelet, s is the scaling factor, and τ is the translating factor. The asterisk in Eq. (5) represents the complex conjugate. The result of CWT is usually presented in the form of power spectral density in the time–frequency domain, which is defined as $|\mathrm{CWT}(s,\tau)|^2$, and termed the CWT spectrogram in the present paper. In the present analysis, the CWT with the Morlet wavelet as mother wavelet is used as suggested by Farge (1992). The Morlet wavelet is expressed as

$$\psi(t) = \pi^{-1/4} \mathrm{e}^{\mathrm{i}\omega_o t} \mathrm{e}^{-t^2/2}. \tag{6}$$

The algorithm proposed by Torrence and Combo (1998) is used to calculate the CWT.

The CWT of a discrete time series can be defined as the convolution of the time series with a scaled and translated version of the mother wavelet, which is carried out in Fourier space using the discrete Fourier transform (DFT). This is implemented by the codes written and performed using the MATLAB software package. Further details concerning the algorithm and its implementation can be found in Torrence and Combo (1998).

In wavelet analysis, the temporal scaling factor s is used rather than the normal frequency employed in conventional Fourier analysis. In order to interpret the results of wavelet analysis in the conventional way, the scaling factor needs to be converted into an equivalent Fourier frequency. The basic idea of conversion is to substitute a single-frequency wave of a known frequency into the wavelet transform and then find the temporal scaling factor at which the wavelet spectrum takes its maximum value. Repeating this procedure for a series of frequencies, the relation between the temporal scaling factor and the equivalent Fourier frequency can be established. For the Morlet wavelet, the relation is given by

$$f = \frac{1}{1.03s}. \tag{7}$$

This is the equivalent Fourier frequency adopted in the present CWT analysis of the calculated time series.

4. Results and discussion

It is difficult to decide what values of Re to specify for the simulations and how many different values are to be calculated in order to fully understand the gap flow behavior and its effect on the flow-induced forces. Based on the brief review given in Section 1, a rough idea of what Re to calculate could be gained. It is observed that for $\mathrm{Re} < 60$, there is no vortex shedding. Consequently, the gap flow behavior is not of interest in the context of the present investigation. On the other hand, a $\mathrm{Re} > 200$ will give rise to transition behavior in the wake. As a result, the flow is not completely laminar in nature as stipulated in the present formulation. Therefore, the resultant Re chosen varies from 60 to 200. Altogether, six different simulations have been carried out; the Re for these six cases is 60, 70, 80, 100, 105 and 200. This choice of Re was decided after numerous simulations have been carried out to explore the change in character of the flow from one Re to the next.

The data thus obtained for these six cases are voluminous and they include the lift and drag time series, the CWT lift and drag spectrograms and instantaneous spectra, and the flow patterns in the form of vorticity plots. In order to make the presentation more coherent so that the salient points of the analysis can be brought out, and to find a way to compare the calculations with the predictions of a theoretical model, a two-step approach is used to analyze the data. The first step is to examine the statistics of the lift and drag time series to identify trends in their distributions within the range of Re investigated. Once the trends are identified, attention is focused on explaining these trends. Therefore, in

the second step, the CWT spectrograms and instantaneous spectra, and the vorticity plots are scrutinized. It is hoped that, through this careful examination of the data, a deeper understanding of the effect of Re for this particular T/D could be gained.

4.1. Behavior of the lift and drag forces

The first and second moments of the lift and drag time series, i.e., the mean and r.m.s. values of the fluctuating forces, are calculated and summarized in Table 1. The mean and r.m.s. values are also plotted in a semi-log scale in Fig. 2 with the force coefficients versus Re. Altogether, there are four plots in Fig. 2, one each for the mean and r.m.s. values of the lift and drag coefficients.

From Table 1 and Fig. 2, two transition regions can be identified, one from $\mathrm{Re} = 70$ to 80, and the other from $\mathrm{Re} = 100$ to 105. The mean lift coefficient $\bar{C}_L$ shows a continuous drop for the upper cylinder and a continuous increase for the lower cylinder. In general, $\bar{C}_L$ is of opposite sign for the upper and lower cylinder and their values are approximately equal, thus indicating that there is no net attractive or repulsive force. However, it is noted that they are slightly different in the range $80 \leqslant \mathrm{Re} \leqslant 100$, with the lower cylinder registering a higher negative $\bar{C}_L$. The maximum difference amounts to ~15% based on $\bar{C}_L$ for the upper cylinder.

In this range, $\bar{C}_D$ for the upper and lower cylinder also shows a significant difference. Over the whole range of Re investigated, the $\bar{C}_D$ shows a drastic drop (>20%), with the upper and lower cylinder registering identical behavior in general. In the range $80 \leqslant \mathrm{Re} \leqslant 100$, however, the lower cylinder $\bar{C}_D$ decreases drastically in the first transition region but increases rapidly in the second transition region. As a result, a significant difference between the upper and lower cylinder is observed.

The behavior of C'_L and C'_D follow a similar trend in the whole range $60 \leqslant \mathrm{Re} \leqslant 200$, namely, a drop in value from $\mathrm{Re} = 70$ to 80, and a very drastic increase from $\mathrm{Re} = 100$ to 105. It should be noted that, in the second transition region, the nature of the force changes from deterministic to random, with the latter showing nonstationary features. Therefore, when plotting the r.m.s. values in the range $105 \leqslant \mathrm{Re} \leqslant 200$, three values at the same Re are presented, a low, a mean, and a high value. All three values show a drastic increase from $\mathrm{Re} = 100$ to 105 and a further increase; from $\mathrm{Re} = 105$ to 200. In the first transition region, a change in the nature of the fluctuating force is not noted.

The flow patterns are examined next to gain understanding of the observed behavior. In the course of analyzing the flow patterns, it is discovered that, as Re is increased from 60 to 200, two transition regions are observed and these two regions coincide with those given by the force statistics discussed above. This suggests that three different flow regimes can be identified. Each regime is associated with a limited range of Re and, as Re crosses from one regime to the next, there are substantial changes in flow patterns and unsteady force characteristics. The three regimes are labeled as Regime I—unbiased gap flow, Regime II—stable biased gap flow, and Regime III—unstable gap flow. The Re associated with these three regimes is 60–70 for Regime I, 80–100 for Regime II, and 105–200 for Regime III.

In the following, attention is focused on the discussion of the transition regions, especially the second region where the flow characteristics change from deterministic to random in addition to drastic increases in C'_L and C'_D. This is then followed by an attempt to compare the present results with those predicted by a theoretical model.

Table 1
Statistics of lift and drag coefficients for all Re investigated

	Regime I—unbiased gap flow				Regime II—stable biased gap flow				Regime III—unstable gap flow*			
Re	60		70		80		100		105		200	
Cylinder	Upper	Lower	Upper	Lower	Upper	Lower	Upper	Lower	Upper	Lower	Upper	Lower
$\bar{C}_D$	1.93	1.93	1.85	1.85	1.64	1.82	1.56	1.69	1.65	1.64	1.54	1.54
$C'_D \times 10^3$	6.23	6.21	21.8	22.4	0.500	0.885	8.21	6.02	70	70	140	130
$\bar{C}_L$	0.51	−0.51	0.48	−0.48	0.41	−0.50	0.39	−0.45	0.41	−0.42	0.36	−0.36
$C'_L \times 10^2$	4.26	4.21	5.65	5.65	0.492	0.113	0.954	0.380	7.0	7.0	23	23
St	0.14	0.14	0.13	0.13	0.10	0.10	0.10	0.10	0.20	0.20	0.20	0.20
	0.14	0.14	0.03, 0.15	0.03, 0.15	0.10	0.10	0.0125, 0.12	0.0125, 0.12	0.10, 0.21	0.10, 0.21	0.21	0.21
	0.14	0.14	0.03, 0.16	0.03, 0.16	0.10	0.10	0.0125, 0.12	0.0125, 0.12	0.23	0.23	0.08, 0.23	0.08, 0.23

*Nonstationary behavior is found in this regime, thus the statistics given here are only representative mean values. See text for details.

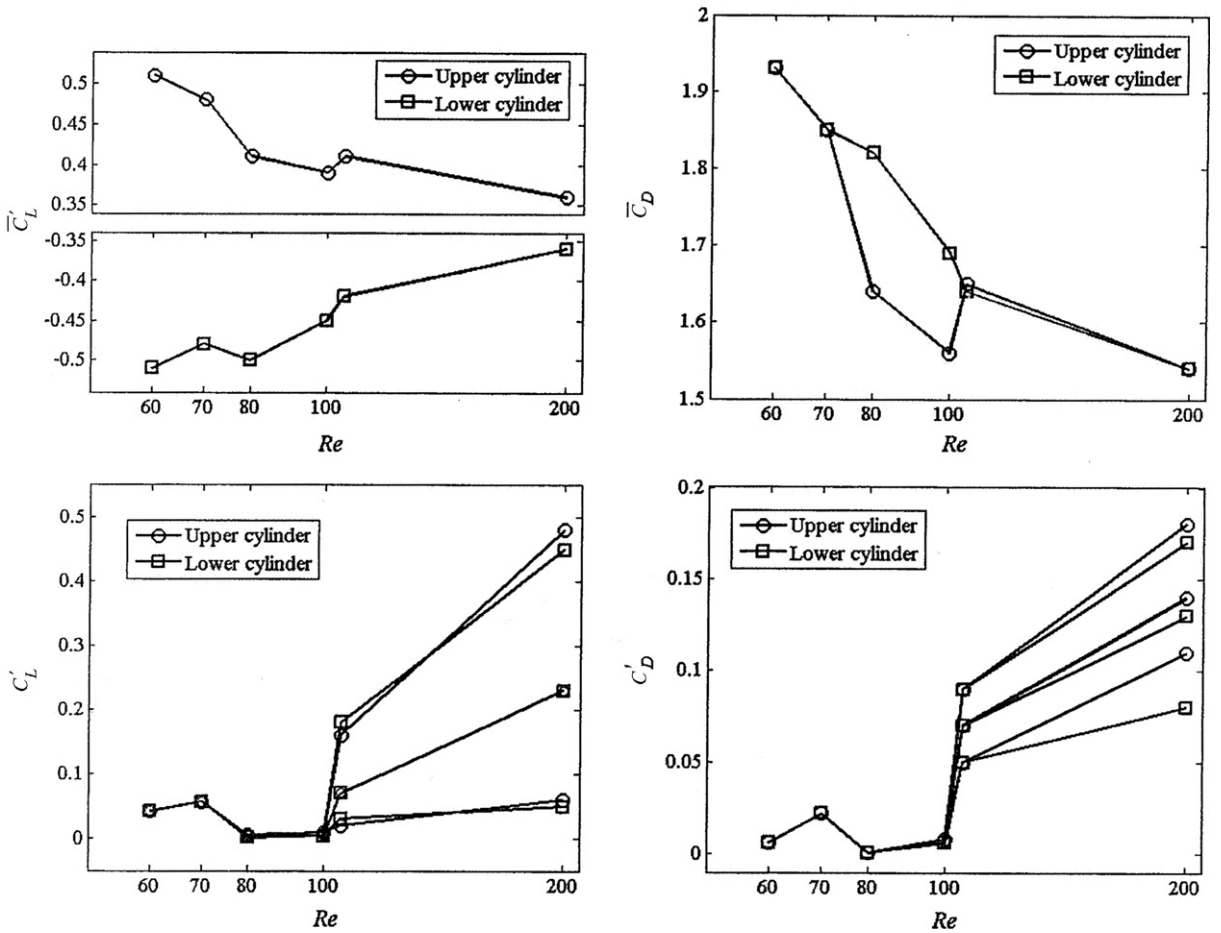

Fig. 2. Plots of mean and root-mean-square values of the lift and drag coefficients versus Re. When the root-mean-square values are time-variant (at Re = 105 and 200), their minimum, mean, and maximum values are plotted.

4.2. Transition from Regimes I to II

This transition occurs between Re = 70 and 80. In Fig. 3, the time histories of the lift and drag at these two Re are shown for comparison. At these two Re, both lift and drag reach steady states after a period of evolution. However, the steady state changes from a multiple-frequency nature at Re = 70 to a single-frequency nature at Re = 80.

More details of the frequency content can be found from their CWT spectrograms shown in Fig. 4. At Re = 70, either the lift or the drag consist of a component at $f = 0.03$ and a component at $f = 0.15$ or 0.16 with periodically varied amplitude. The periodicity in the time histories is actually the result of the superposition of these two components. For the lift coefficient, the component at $f = 0.15$ is dominant. For the drag coefficient, the component at $f = 0.03$ is dominant. The CWT spectrograms at Re = 80 appear to be relatively simple; either the lift or the drag has a single component at $f = 0.10$. Unlike those at Re = 70, however, the amplitudes for the two cylinders show obvious differences. This is consistent with the mean and r.m.s. values given in Table 1.

A zoomed view of the CWT spectrograms at Re = 70 is given in Fig. 5. One salient feature is that the component of the lift at $f = 0.15$ and the component of drag at $f = 0.16$ have periodically varied dominant frequencies. Instantaneous CWT spectra at selected times are also given in Fig. 5. It can be seen that the component of lift varies its dominant frequency from $f = 0.15$ to 0.14 and 0.21 in a periodic way, and the component of drag has similar behavior. Moreover, the frequency of such variation is approximately equal to $f = 0.03$, the frequency of another component.

In order to unveil the underlying physics of this feature, vorticity plots from $t = 314$ to 350 are calculated, and three of them are selected for presentation in Fig. 6. It can be seen that two vortex streets are formed in the near wake of the

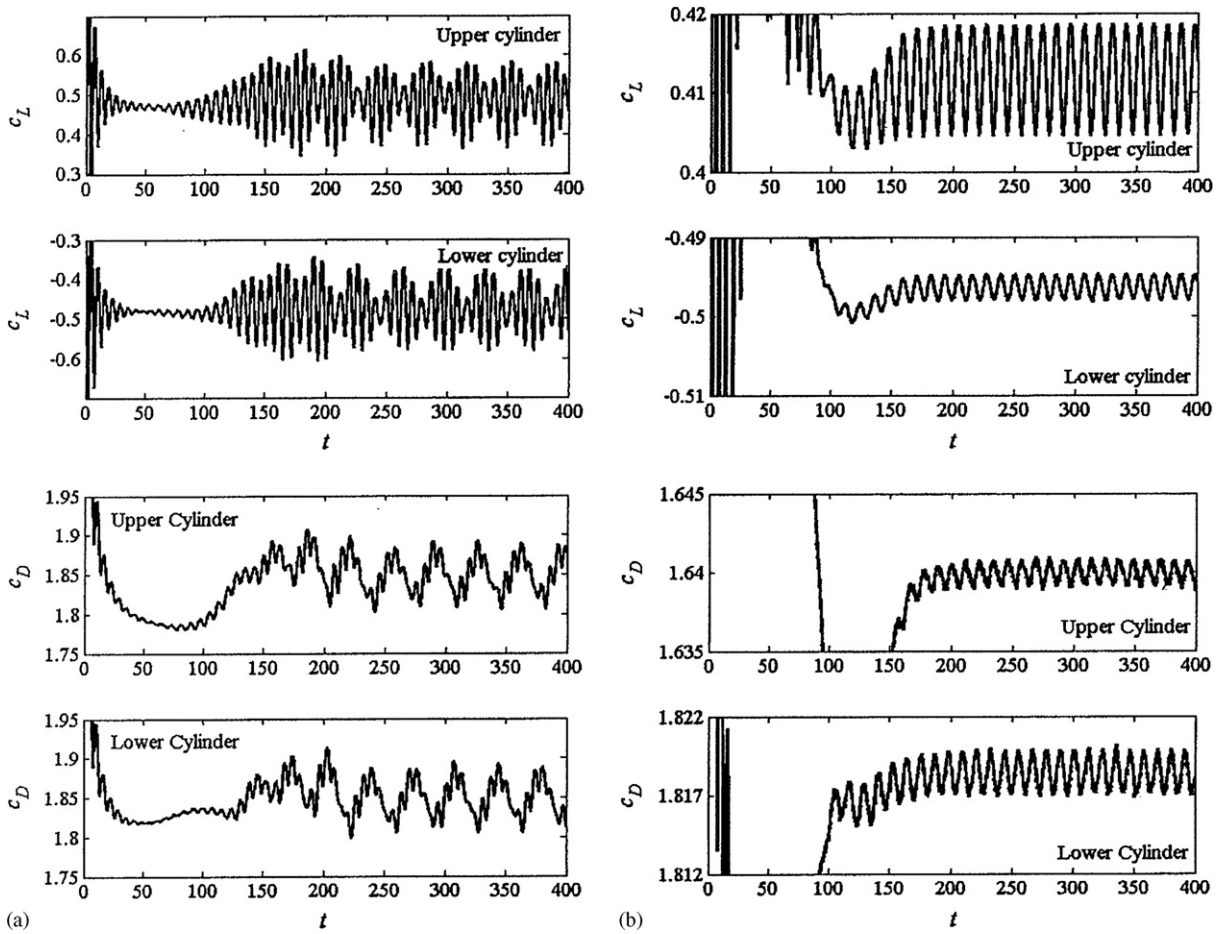

Fig. 3. Time histories of the lift and drag coefficients: (a) Re = 70; and (b) Re = 80.

two cylinders, and a gap flow exists between them. When the vortices develop further, only the outer vortices travel to the far wake and result in a single vortex street. The outer vortices restrict the development of the inner vortices. As a result, the inner vortices become weak and eventually disappear in the middle section of the wake. Due to the influence of the inner vortices, the initially unbiased gap flow becomes fluctuating. The inner vortices show a different pattern of shedding. In the very near wake, two positive vortices are shed from the upper cylinder consecutively. This is followed by a state where a positive vortex and a negative vortex coexist as seen from the flow pattern at $t = 326$; this state ends with a positive vortex shed from the upper cylinder. Afterwards, two negative vortices are shed from the lower cylinder consecutively, and this is followed by a state of coexistence. This time, however, a negative vortex is shed from the lower cylinder to end the state, and finish one cycle of inner vortex shedding. The period of this cycle is $T = 36$, thus the frequency of inner vortex shedding is $f = 0.028$, which is roughly the frequency of the low-frequency component of either the lift or the drag. It can thus be concluded that the interference between the inner vortices shed from the two cylinders induces a low-frequency force component in both the lift and the drag, and this component dominates the drag. The interference also affects the force component due to the single vortex street by modulating its amplitude and dominant frequency, resulting in a periodic behavior.

In this transition region, the gap flow changes from an unbiased state at Re = 70 to a biased state at Re = 80 as shown in Fig. 7. The gap flow is always biased towards the lower cylinder, and this is responsible for the differences noted between the upper and lower cylinders in the distribution of $\bar{C}_L$ and $\bar{C}_D$. Due to the biased gap flow, the negative inner vortex shed from the lower cylinder is suppressed, while the positive inner vortex shed from the upper cylinder develops in the middle section of the wake. However, it does not move towards the far wake. Only a single vortex street consisted of the outer vortices develops in the far wake.

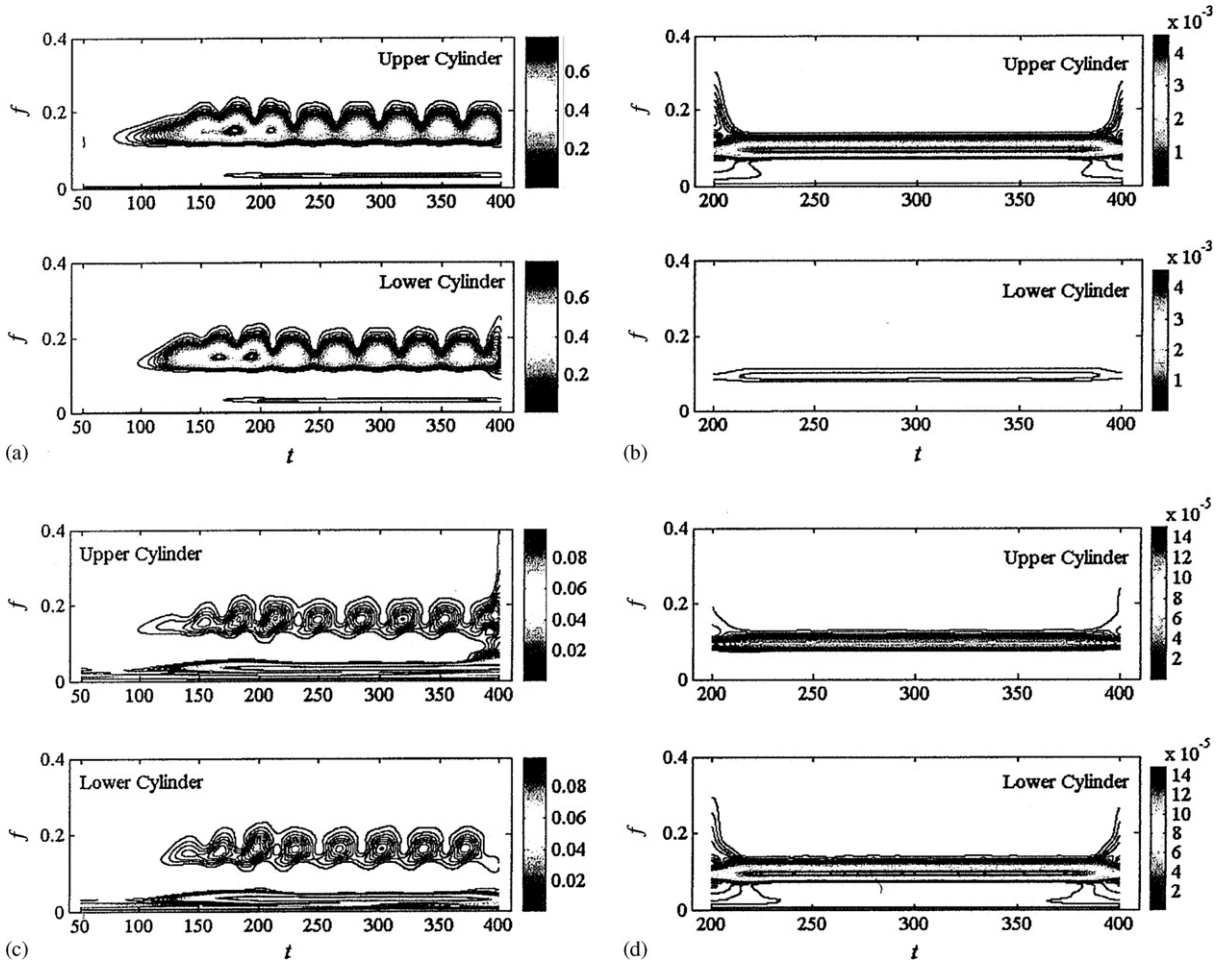

Fig. 4. CWT spectrograms of the lift and drag coefficients: (a) lift at Re = 70; (b) lift at Re = 80; (c) drag at Re = 70; and (d) drag at Re = 80.

4.3. Transition from Regimes II to III

Different from the previous transition region, this one changes from a deterministic state to a stochastic one, as indicated by the time histories of both the lift and the drag shown in Fig. 8. The deterministic state at Re = 100 appears to be a further development of that at Re = 80 by incorporating the features at Re = 70, i.e., the gap flow is now biased and the interference between the inner vortices induces low-frequency components in both the lift and the drag. On the other hand, the stochastic state at Re = 105 shows some nonstationary features; both the dominant frequency and the amplitude vary with time significantly. Therefore, the statistics given in Table 1 are only representative values. It should be mentioned that the minimum, mean, and maximum values of the time-variant r.m.s. values are plotted in Fig. 2 to demonstrate the nonstationary nature of the forces.

Detailed changes of the frequency content during the transition can be observed from the CWT spectrograms shown in Fig. 9. At Re = 100, either the lift or the drag consists of a component at $f = 0.012$ with constant amplitude and a component at $f = 0.12$ with periodically varied amplitude. The periodicity in the time histories is actually the result of the superposition of these two components. For C_L, the components at $f = 0.012$ and 0.12 are equally dominant. For C_D, only the component at $f = 0.012$ is dominant. Moreover, the amplitudes of the lift and the drag are different for the two cylinders, implying that the gap flow is now biased. This is confirmed by typical vorticity plots shown in Fig. 10. It can be seen that the gap flow is always biased towards the lower cylinder. The outer vortices form a single vortex street in the far wake, while the inner vortex shed from the lower cylinder is suppressed and that from the upper cylinder develops to the middle section of the wake. As a result, the C'_L and C'_D are different for the two cylinders.

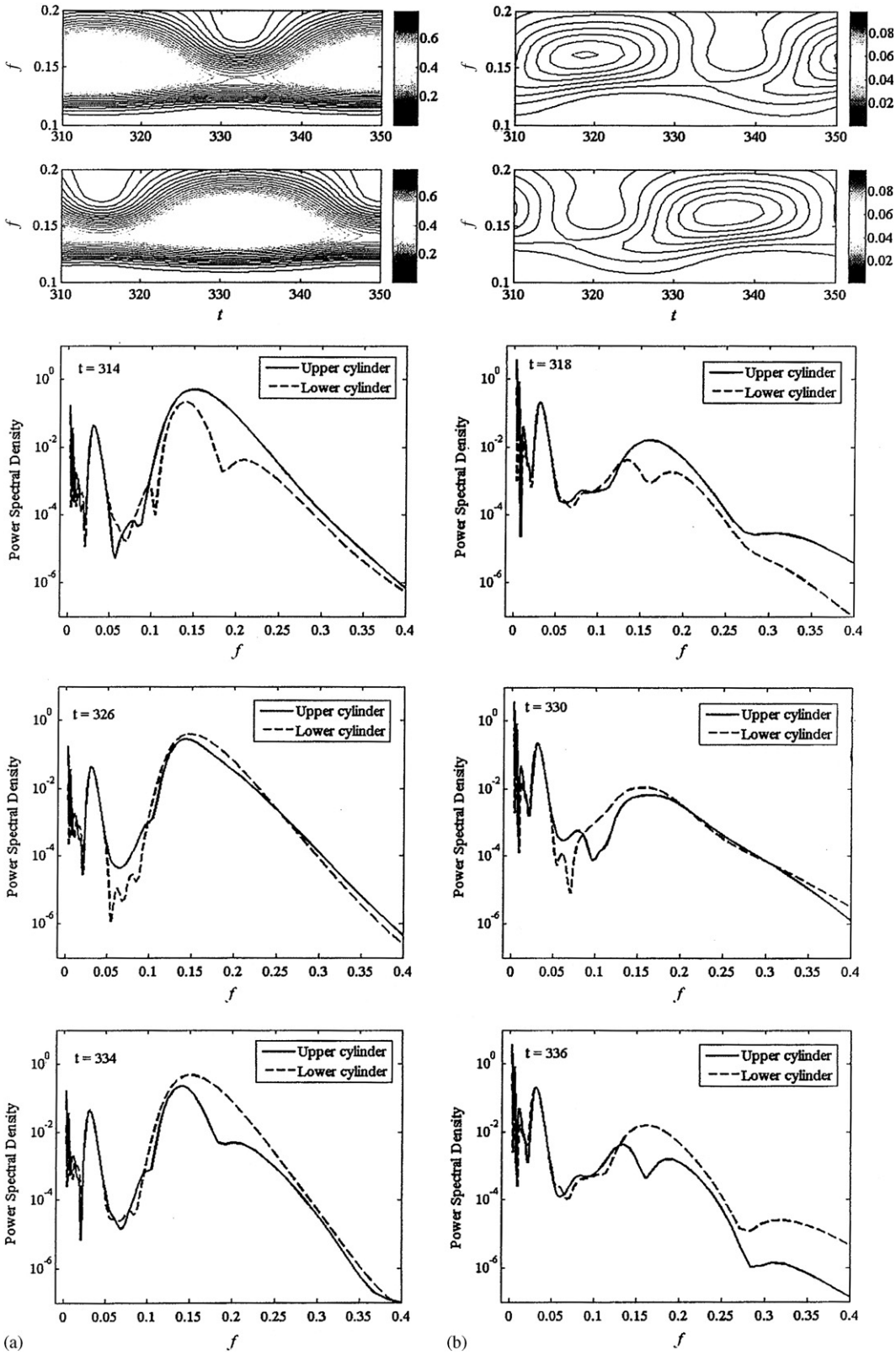

Fig. 5. Zoomed view of CWT spectrograms and selected instantaneous CWT spectra at Re = 70: (a) lift; and (b) drag.

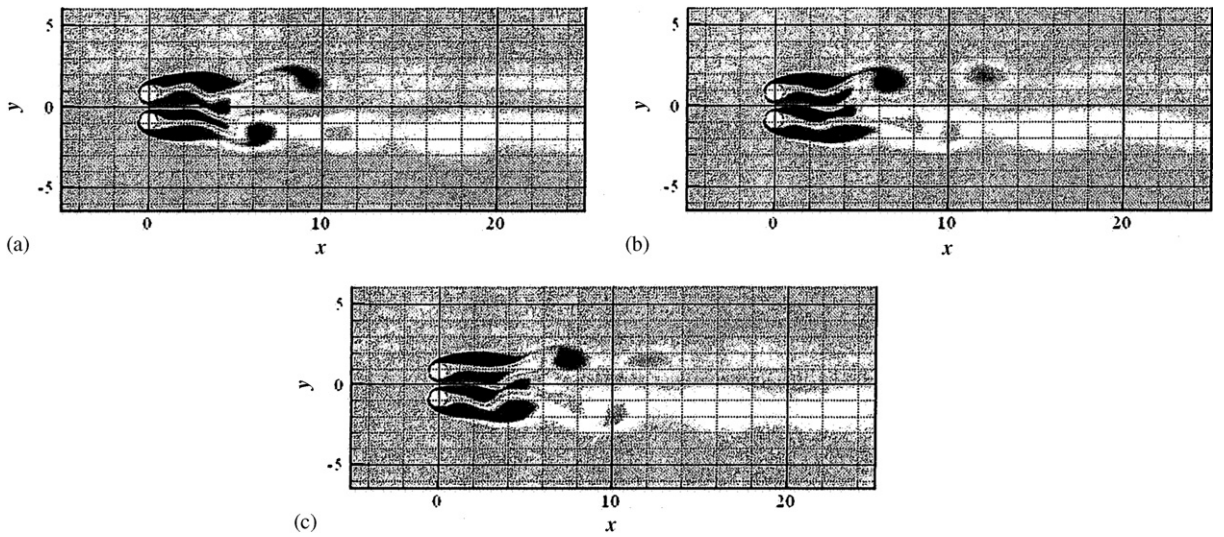

Fig. 6. Vorticity plots at selected times at Re = 70: (a) $t = 314$; (b) $t = 326$; and (c) $t = 334$.

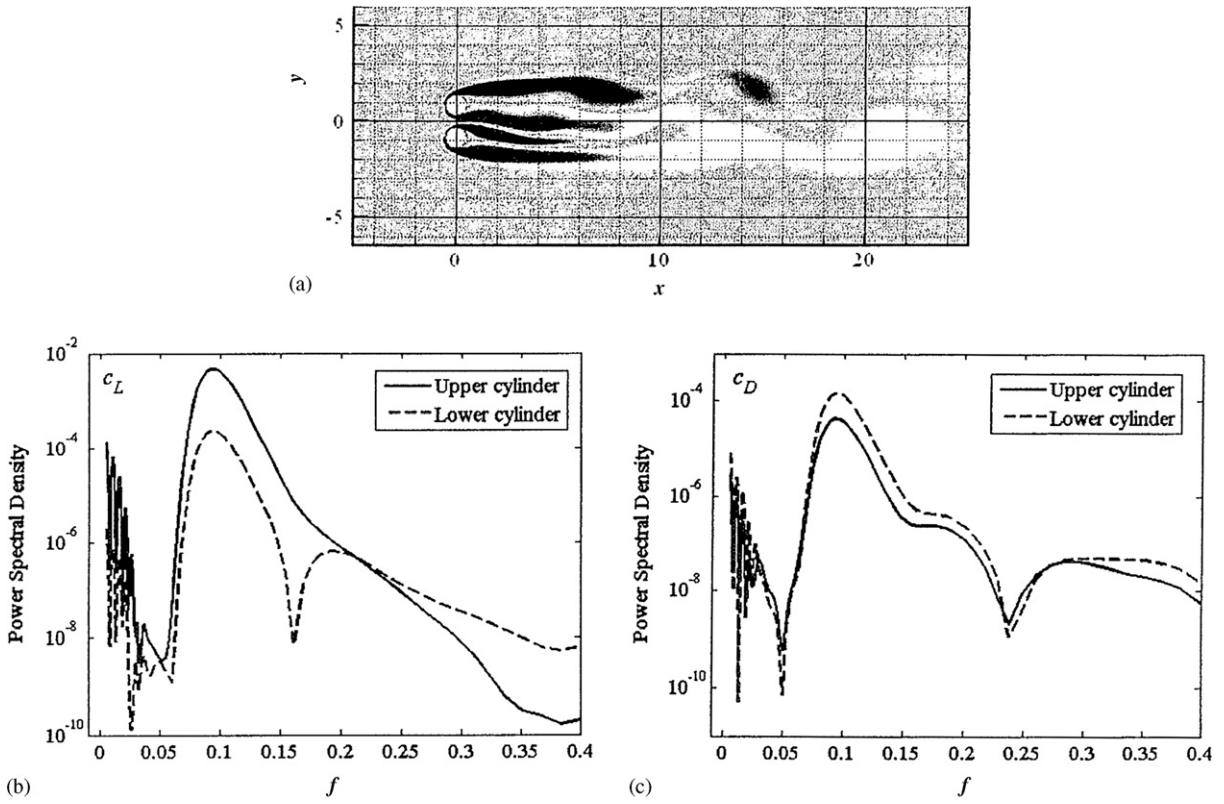

Fig. 7. A typical vorticity plot and the corresponding instantaneous CWT spectra of the force coefficients at Re = 80 and at $t = 300$: (a) vorticity plot; (b) instantaneous CWT lift spectrum; and (c) instantaneous CWT drag spectrum.

The low-frequency component at $f = 0.012$ suggests that the inner vortex shedding has a frequency 1/10 of that of the outer vortex shedding. This is different from the case at Re = 70, where the frequency of the inner vortex shedding is 1/5 of that of the outer vortex shedding. Vorticity plots for two time segments, one from $t = 617$ to 627 and the other from

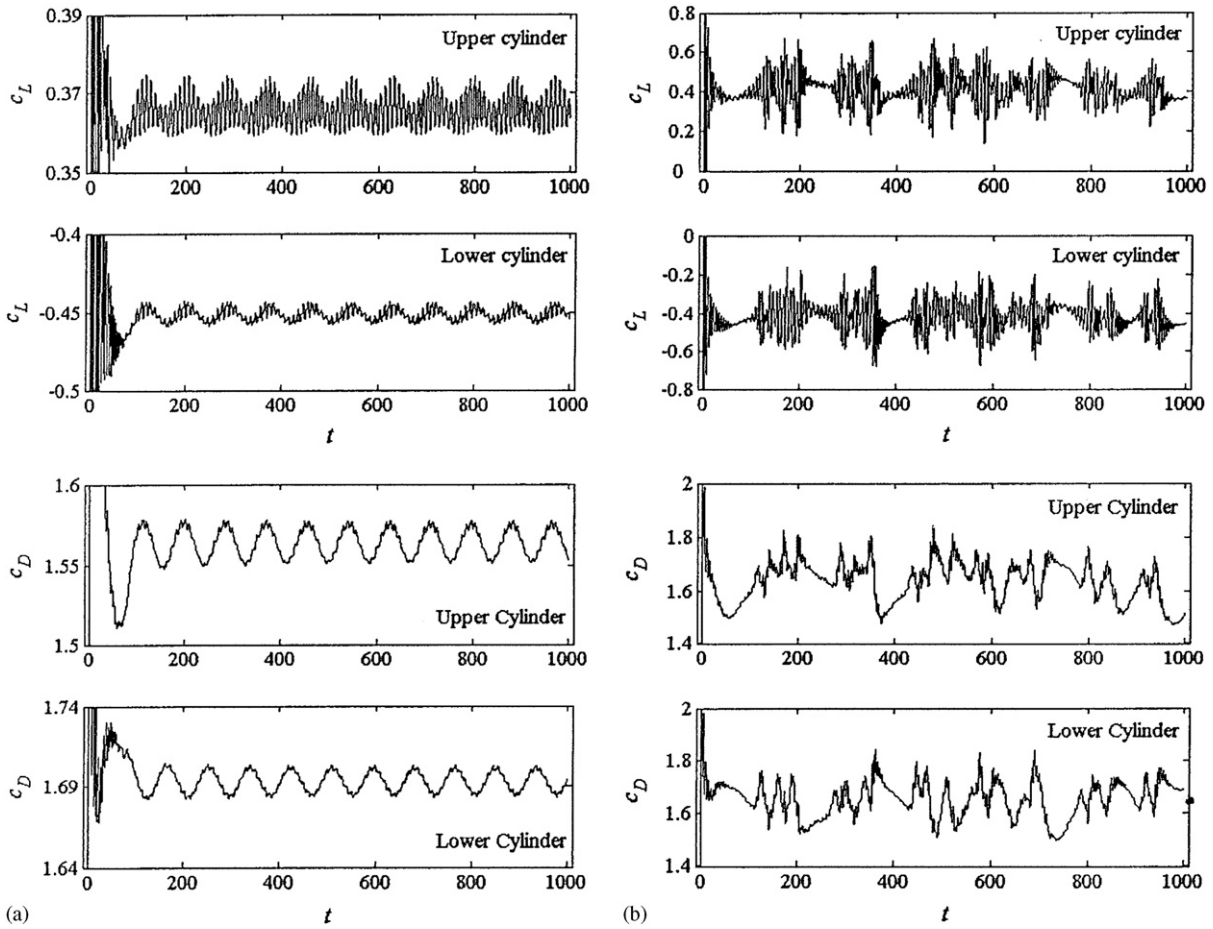

Fig. 8. Time histories of the lift and drag coefficients: (a) Re = 100 and (b) Re = 105.

$t = 656$ to 666, are examined in an attempt to understand the pattern of inner vortex shedding at the given Re. It is found that the inner vortex shedding essentially has an identical pattern to that of the outer vortex shedding. Nevertheless, a comparison of the vorticity plots at $t = 622$ and $t = 661$ as given in Fig. 10, at which local maximum values of lift are observed, shows that there is a minor difference. The vortex shedding at $t = 622$ is slightly stronger than that at $t = 661$. However, the variation is so small (approximately 5% of the amplitude) that it cannot be identified from the flow patterns alone. The CWT spectrograms need to be used as guidelines.

Instantaneous CWT spectra at $t = 622$ and $t = 661$ are also given in Fig. 10. At $t = 622$, the periodically variant component of the lift takes its maximum value. For the upper cylinder, the dominant frequencies occur at $f = 0.012$ and 0.12. For the lower cylinder, there are three dominant frequencies locating at $f = 0.012$, 0.12 and 0.21. The drag shows similar behavior, except that the $f = 0.012$ component is dominant. At $t = 661$, the periodically varied component of the lift takes its minimum value. For the upper cylinder, the dominant frequency changes to $f = 0.10$, while for the lower cylinder there are only two dominant frequencies, one at 0.10 and another at 0.22. For the drag, the dominant frequency of the periodically varied component also changes to 0.10 for the upper cylinder, but the dominant frequencies for the lower cylinder remain unchanged.

At Re = 105, the frequency content of either the lift or the drag are dominated by narrow-band components, and they are time-variant in a quasiperiodic way. The central frequency of the narrow band components is around $f = 0.20$. Referring to the time histories, it can be seen that the quasiperiodic behavior is due to a change between large-amplitude and low-amplitude parts. Two sections of the force coefficient data, one from $t = 300$ to 500 and the other from $t = 660$ to 840, are selected for detailed study. In the low-amplitude parts, there is almost no fluctuation in either the drag or the lift for both cylinders. However, the variations of the low-amplitude parts of these two sections show opposite trends. In the time segment, $t = 300$ to 500, the mean drag of the lower cylinder decreases while that of the upper cylinder

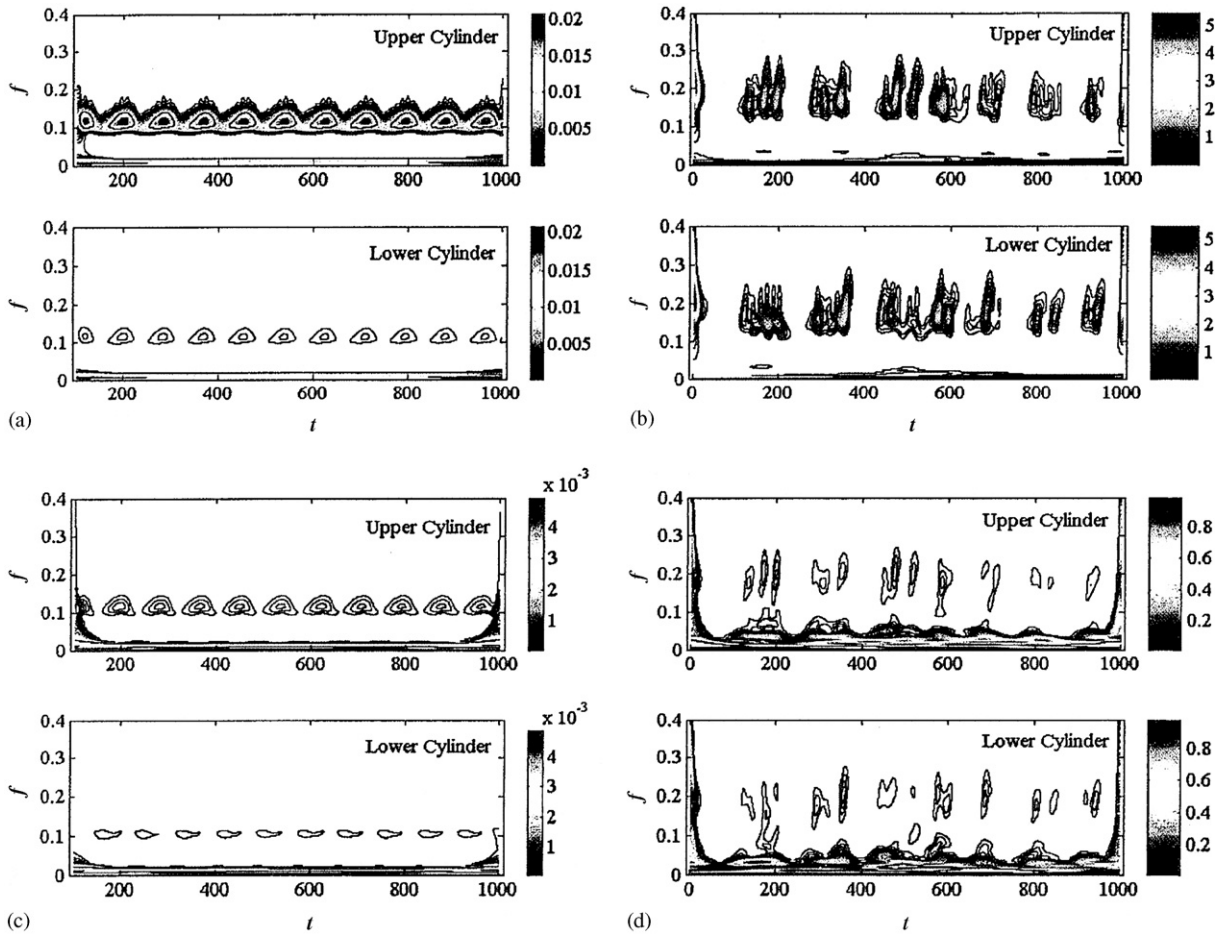

Fig. 9. CWT spectrograms of the lift and drag coefficients: (a) lift at Re = 100; (b) lift at Re = 105; (c) drag at Re = 100; and (d) drag at Re = 105.

increases, and the mean values of the lift for both cylinders appear to increase slightly. In the time section, $t = 660$–840, the mean drag of the lower cylinder decreases while that of the upper cylinder increases, and the mean values of the lift for both cylinders appear to decrease slightly.

Flow patterns corresponding to these two segments are calculated in an attempt to understand the underlying physics. Firstly, typical vorticity plots corresponding to the low-amplitude part ($t = 400$ and 750) are plotted in Fig. 11. Instantaneous CWT spectra are also given. For the low-amplitude part, the gap flow is biased towards either the upper or the lower cylinder. For the cylinder with a wide wake, the dominant frequency of vortex shedding is around $f = 0.1$; for the cylinder with a narrow wake, two dominant frequencies: one around $f = 0.1$ and the other around $f = 0.2$, are observed.

An interesting phenomenon is found from the vorticity plots during the transition between the large-amplitude parts and the low-amplitude parts, as shown in Fig. 12. At $t = 368$, the inner vortex shed from the upper cylinder is amalgamated with the outer vortex shed from the lower cylinder, and moves to the outer vortex street. This is consistent with the flow pattern at $t = 400$ shown in Fig. 11(a), where the gap flow is biased towards the lower cylinder. At $t = 680$, it is the inner vortex shed from the lower cylinder that is amalgamated with the outer vortex shed from the upper cylinder, and moves to the outer vortex street. This is consistent with the flow pattern at $t = 750$ shown in Fig. 11(b), where the gap flow is biased towards the upper cylinder.

The amalgamation of the inner and the outer vortices suggests that the flow interference between the two cylinders extends its influence to the outer vortices. As a result, normal vortex shedding of outer vortices is disturbed, and flow-induced forces have a significant change in both the frequency content and the amplitude. Such disturbances appear in a random way, hence the vorticity plot also shows random variation between the state of unbiased-gap-flow and the state

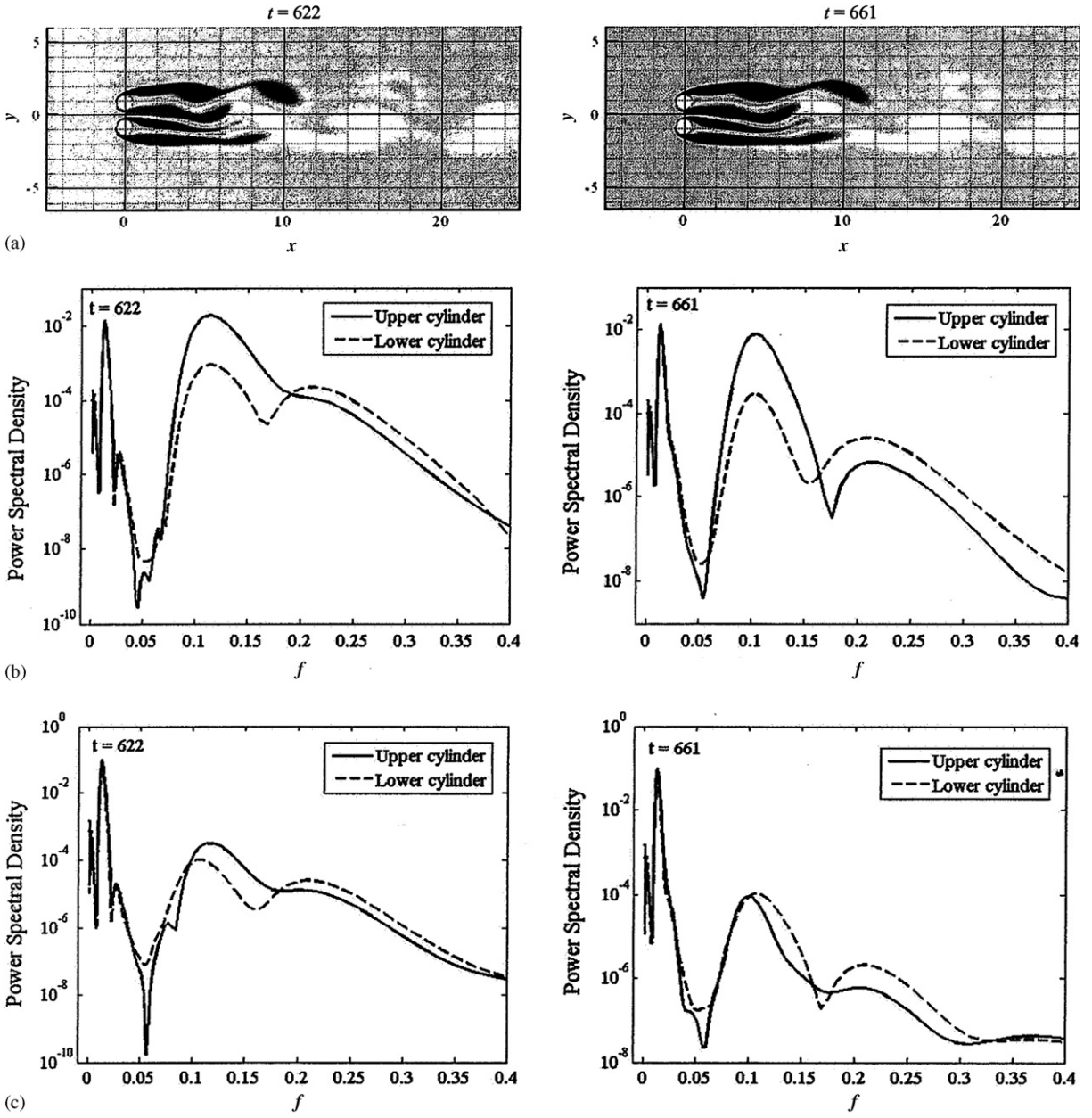

Fig. 10. Typical vorticity plots and the corresponding instantaneous CWT spectra of the force coefficients at Re = 100 and at $t = 622$ and 661: (a) vorticity plots; (b) instantaneous CWT lift spectra; and (c) instantaneous CWT drag spectra.

of biased-gap-flow, and the flow-induced forces show some nonstationary features as indicated by the CWT spectrograms. From the corresponding instantaneous CWT spectra, it can be seen that the frequency bands of the force coefficients become rather wide. Also, the r.m.s. values are very large compared with those at Re = 100 as shown in Table 1. These features make flow-induced vibration much easier to be excited, and the amplitude of vibration is expected to be large. Therefore, particular attention should be paid to this transition region in practical design of engineering systems involving cylinder arrays appearing in a side-by-side configuration.

Numerical simulations at several higher Re's up to Re = 200 are also carried out. In general, similar behavior is observed. Moreover, it is found that when Re is increased, the interaction between the inner vortices and the outer vortices becomes strong, and normal vortex shedding is destroyed further. This can be seen from the results obtained at

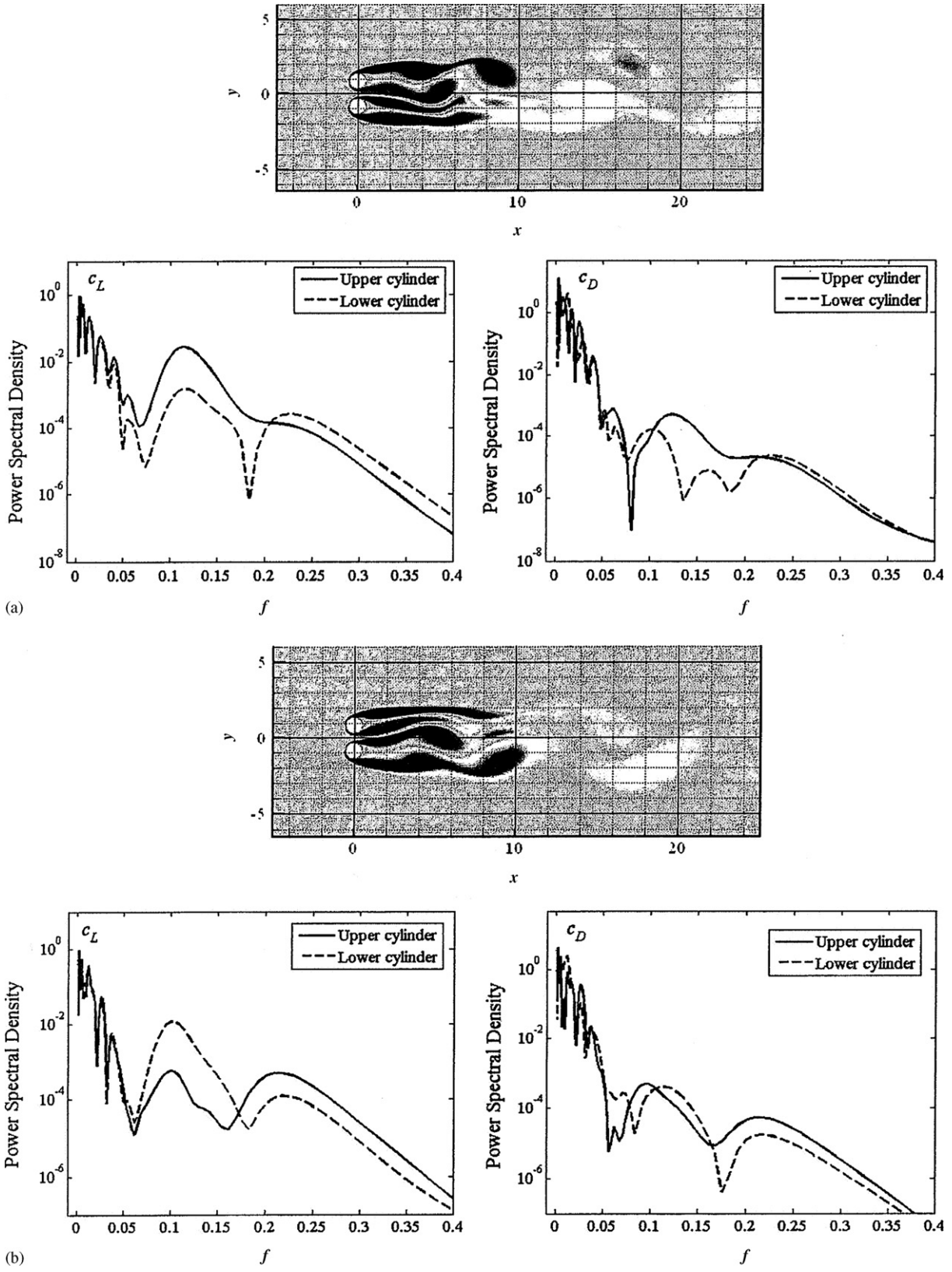

Fig. 11. Vorticity plots corresponding to the low-amplitude parts of the time histories and the corresponding instantaneous CWT spectra of force coefficients at Re = 105: (a) $t = 400$; and (b) $t = 750$.

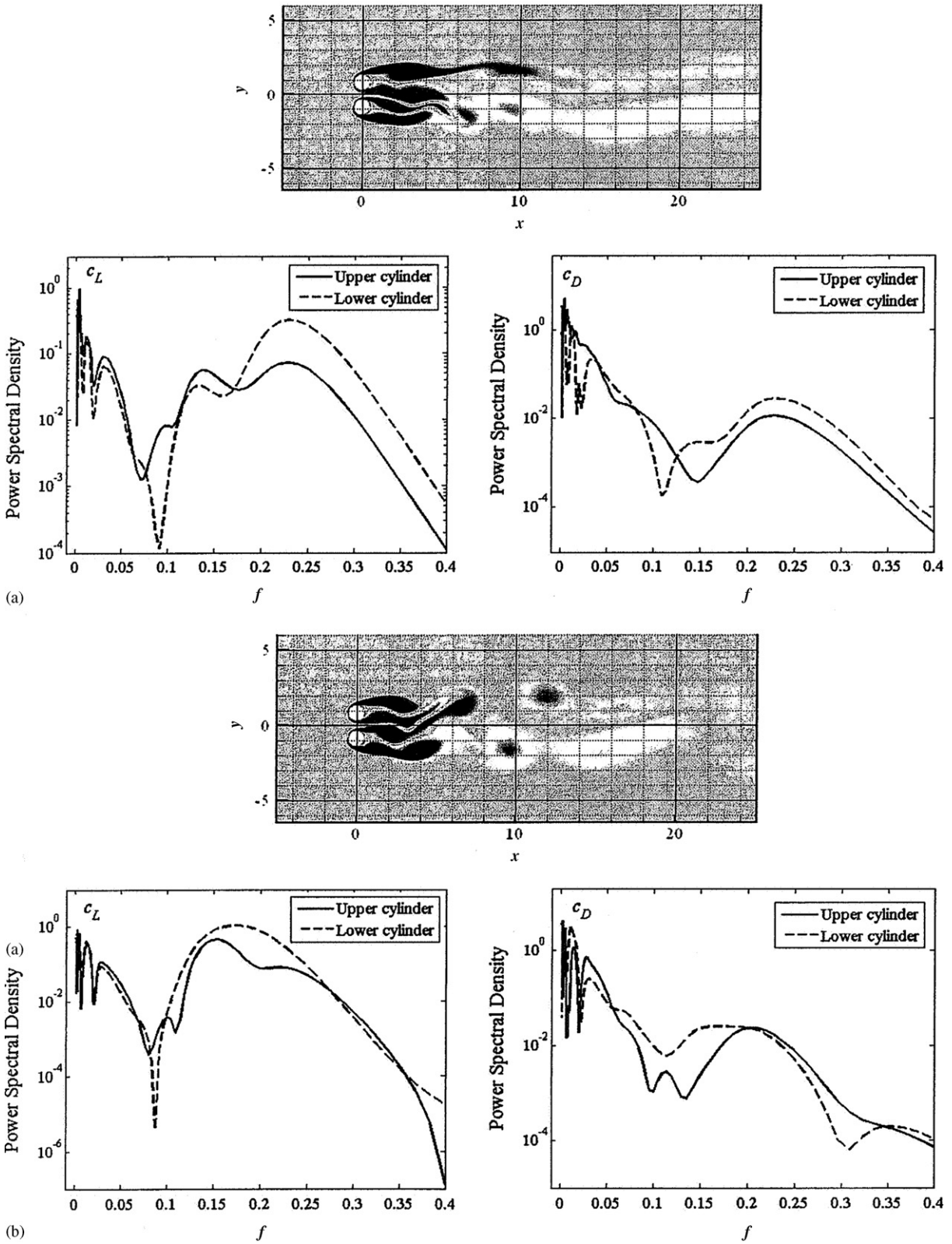

Fig. 12. Instantaneous CWT spectra of the force coefficients and the corresponding flow pattern at Re = 105: (a) $t = 368$; and (b) $t = 680$.

$Re = 200$. The calculated lift and drag coefficients are plotted in Fig. 13, along with the corresponding CWT spectrograms. Except for a short-time segment from $t = 960$ to 1000, the force coefficients vary with time randomly but appear to be stationary.

A typical vorticity plot is shown in Fig. 14, along with the corresponding instantaneous CWT spectra. It can be seen that the amalgamation of inner vortices with outer vortices is more pronounced, and the single vortex street becomes rather irregular. Accordingly, the spectra of force coefficients show random variation with time. It should be noted that the phenomenon of vortex amalgamation in this regime is consistent with experimental observation for two side-by-side cylinders with pitch ratio $T/D = 1.85$ at $Re = 200$ (Williamson, 1985).

4.4. Comparison with previous studies

From the above discussion, it can be seen that the two critical transition regions are two boundaries separating three flow regimes in the range $60 \leqslant Re \leqslant 200$. According to the features shown by the vorticity plots, these three regimes are defined as Regime I—unbiased gap flow, Regime II—stable biased gap flow, and Regime III—unstable gap flow.

Since the present simulation is carried out in a low Re range, it could not be directly compared with experimental measurements which were usually obtained at higher Re, except for the experiment of Williamson (1985). Nevertheless, the present simulation reproduces the biased gap flow and associated change of St. Strong bistable gap flow is not found, but the results at $Re = 200$ have shown some features of flip-flop. It is suspected that the bistable gap flow may become strong enough to be identified at higher Re. This is partially supported by numerical simulations at relatively high Re (Chen et al., 2003; Jester and Kallinderis, 2003).

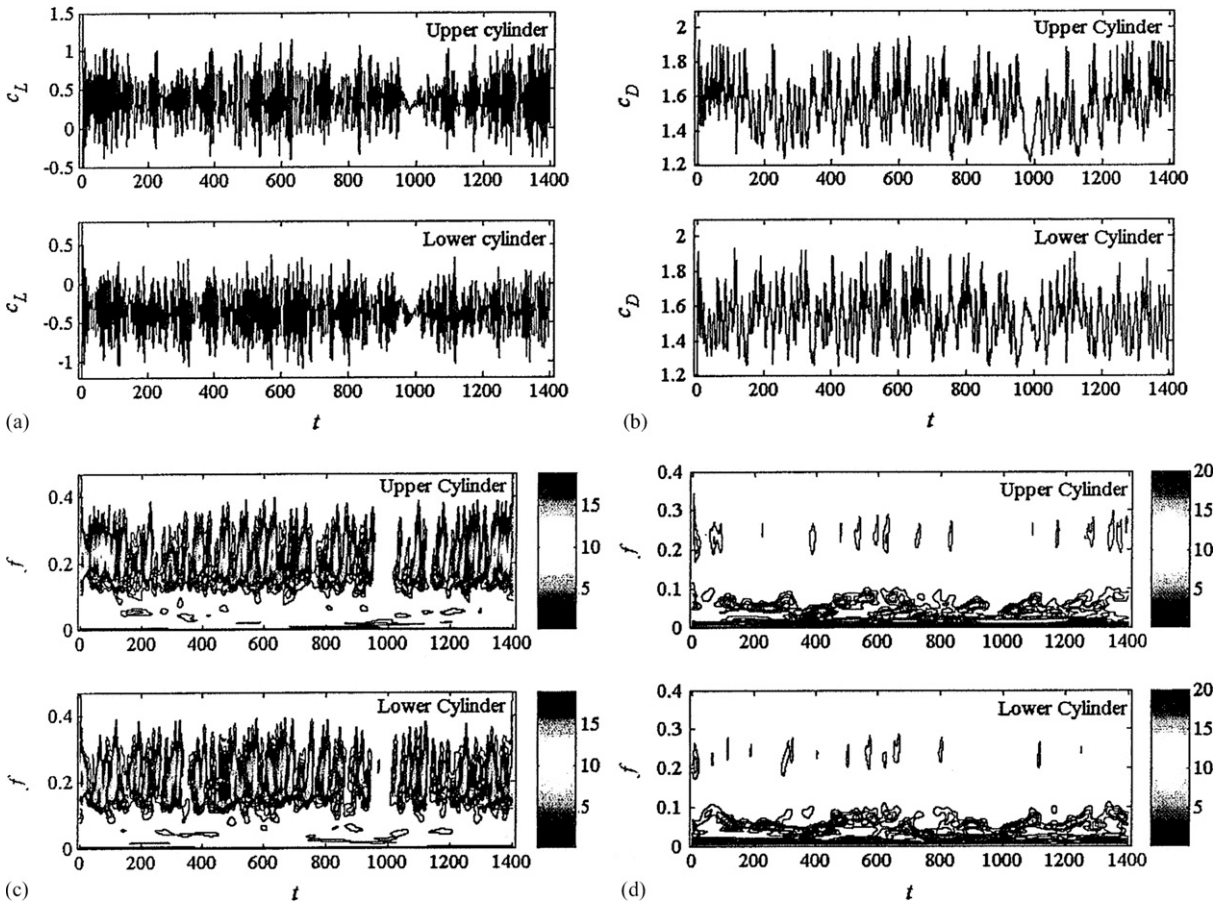

Fig. 13. Time histories of the force coefficients and the corresponding CWT spectrograms at $Re = 200$: (a) lift; (b) drag; (c) CWT lift spectrogram; and (d) CWT drag spectrogram.

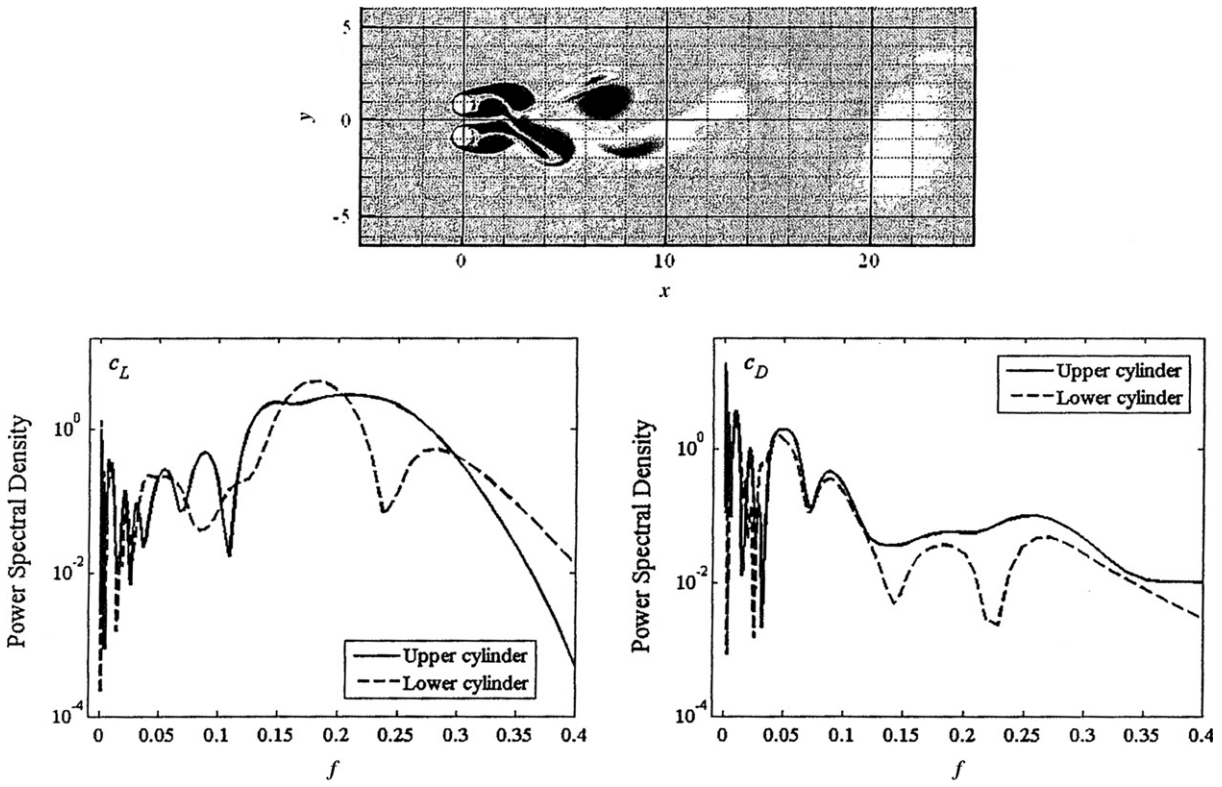

Fig. 14. Typical vorticity plot and the corresponding instantaneous CWT spectra of the force coefficients at Re = 200 and $t = 680$.

On the other hand, the present simulation shows good agreement with previous numerical results. The flow patterns at Re = 100 are similar to the single combined wake reported by Chang and Song (1990). The difficult-to-identify frequency peaks (Ng et al., 1997) could be attributed to the time-variant frequency content, as shown by the present wavelet analysis. As a result, the frequency peak appears to be of narrow-band with a smooth central peak which is similar to that described by Meneghini et al. (2001).

Furthermore, it is reviewed in the Introduction that a theoretical model based on the Landau equation has been developed for two side-by-side cylinders in a cross-flow, giving a physical interpretation of the behavior of wake interference (Peschard and Le Gal, 1996). The model predicts that, for a given pitch ratio, the wake undergoes four flow regimes as Re increases, i.e., the regimes of in-phase locking, asymmetric locking, quasi-periodic oscillations, and phase-opposition locking. Based on the flow patterns observed in the experiment, a diagram was also given to show the boundaries of these flow regimes in the range of Re = 90–150 and $T/D = 1.64$–3.33. By comparing the flow patterns described by Peschard and Le Gal (1996) and those obtained from the present numerical simulation, the in-phase-locking regime, asymmetric regime, and quasiperiodic regime are found to correspond to Regimes I–III of the present study, and the regime of phase-opposition does not appear in the Re range considered. For the pitch ratio $T/D = 1.7$, Peschard and Le Gal (1996) showed that transitions occur at Re = 100 and 126, while the present numerical simulation shows that transition occurs at Re = 70–80 and Re = 100–105. This might be due to the fact that, in the model of Peschard and Le Gal (1996), vortex shedding was considered to appear at Re = 90, while the present simulation shows that it appears at Re = 60.

Moreover, the present simulation provides more details for an understanding of the underlying physics of wake interference. In Regime I, the present results show that the spectra of both lift and drag change from constant to periodic as Re increases. Flow patterns show that this is due to the fluctuation of the gap flow, which is a result of the interference of the inner vortices. Similar to Regime I of unbiased gap flow, the lift and drag in Regime II also show a change from constant to periodic as Re increases, due to the fluctuation of the gap flow arising from the interference of the inner vortices. However, the amplitudes for the upper and the lower cylinders are different since the gap flow is now biased.

In Regime III, the present simulation gives a more detailed description of the nonstationary behavior related to the amalgamation of the inner vortices and the outer vortices, and shows that, with increasing Re, the time histories in general will approach stationary behavior. The dominant frequency of the lift and drag force is now narrow-band varying in the range of $f = 0.1$–0.2. The St is also within this range. Although experimental measurements of the dominant frequencies in the near wake or of the flow-induced forces at low Re's are not available for direct comparison, some experimental results at higher Re for the same pitch ratio are noteworthy. Williamson (1985) summarized available experimental hot-wire measurements, showing that the dominant frequencies in the wake are about 0.1 and 0.2, and occasionally appear at 0.3. The range of Re is from 2×10^4 to 3×10^4. At $\mathrm{Re} = 5.5 \times 10^4$, Alam et al. (2003) found that there are three major modes in the near wake: the high-frequency mode where the wake is narrow with a dominant frequency around 0.3, a low-frequency mode where the wake is wide with a dominant frequency about 0.1, and an intermediate-frequency mode with a dominant frequency ~0.2. These three modes interchange in a random way. The present numerical results are consistent with these experimental measurements. In general, the present simulation results are in agreement with the predictions of the theoretical model formulated based on the Landau equation.

5. Conclusions

Numerical simulations of two side-by-side stationary circular cylinders with $T/D = 1.7$ have been carried out in the range of laminar flow ($0 < \mathrm{Re} \leqslant 200$). The calculated lift and drag coefficients are analyzed using the method of CWT to investigate the effect of Re on flow-induced forces. Vorticity plots are calculated from the data of flow velocity to demonstrate the underlying physics of flow interference between two cylinders.

It is found that the effect of Re is significant. For $T/D = 1.7$, the statistics of flow-induced force show two critical transition regions; one from $\mathrm{Re} = 70$ to 80, and the other from $\mathrm{Re} = 100$ to 105. The latter transition region is particularly noteworthy, since the fiow-induced forces show significant increment in amplitudes and band widening in frequency contents. Referring to the vorticity plots, these two transition regions are boundaries separating three flow regimes: (I) the regime of unbiased gap flow ($60 \leqslant \mathrm{Re} \leqslant 70$); (II) the regime of stable biased gap flow ($80 \leqslant \mathrm{Re} \leqslant 100$); and (III) the regime of unstable gap flow ($105 \leqslant \mathrm{Re} \leqslant 200$).

In Regime I, the interference between the two cylinders is limited to the inner vortices, and a normal single vortex street is formed by the outer vortices. Both the lift and the drag are dominated by the components at the frequency of vortex shedding, and their amplitudes are equal for the two cylinders. The gap flow is unbiased in general, except for slight flip-flopping in its front part due to evolution of the inner vortices. At lower Re in this regime, the inner vortices evolve at the frequency of vortex shedding, and have no influence on the lift and the drag. At higher Re close to the transition region, however, the inner vortices have their own pattern of evolution, whose frequency is a fraction of the frequency of vortex shedding. This introduces a low-frequency component in both the lift and the drag, and the total lift and drag appear to be the superposition of this low-frequency component and the normal vortex shedding component.

In Regime II, the interference between the two cylinders is still limited to the inner vortices, and a normal single vortex street is formed by the outer vortices. However, the gap flow is biased towards the lower cylinder, and the evolution of the inner vortex behind the lower cylinder is suppressed. Both the lift and the drag are still dominated by the components at the frequency of vortex shedding, but their amplitudes are not equal for the two cylinders due to the biased gap flow. At lower Re in this regime, the evolution of the inner vortex does not affect the lift and the drag. At a Re close to the transition boundary, a low-frequency component is found in both the lift and the drag, and the total lift and drag appear to be the superposition of this low-frequency component and the normal vortex shedding component. Interestingly, the inner vortex does not show a different pattern of evolution as in Regime I.

In Regime III, the flow interference shows a totally different pattern. It is seen that the flow interference is extended to the outer vortices due to the amalgamation of the inner and the outer vortices. A single vortex street can still be observed, but becomes more and more irregular with increasing Re. The gap flow is unstable due to the random evolution of the inner vortices. Both the lift and the drag appear to be random accordingly; their amplitudes vary with time significantly, and the bandwidths of their dominant components are increased. At lower Re in this regime, the flow appears to vary between a state of unstable gap flow and a state of biased gap flow (towards either the upper or the lower cylinder), in a random way. The lift and the drag show corresponding variations. At higher Re in this regime, the state of biased gap flow is seldom observed, and the flow is essentially in the state of unstable gap flow. Accordingly, the lift and the drag appear to be random and nonstationary to certain degree.

Acknowledgments

Funding support from the Research Grants Council of the Government of the HKSAR under Projects PolyU5307/03E and PolyU5321/04E are gratefully acknowledged.

References

Alam, M.M., Moriya, M., Sakamoto, H., 2003. Aerodynamic characteristics of two side-by-side circular cylinders and application of wavelet analysis on the switching phenomenon. Journal of Fluids and Structures 18, 325–346.

Bearman, P.W., Wadcock, A., 1973. The interaction between a pair of circular beams normal to a stream. Journal of Fluid Mechanics 61, 499–511.

Chang, K.-S., Song, C.-J., 1990. Interactive vortex shedding from a pair of circular cylinders in a transverse arrangement. International Journal for Numerical Methods in Fluids 11, 317–329.

Chen, L., Tu, J.Y., Yeoh, G.H., 2003. Numerical simulation of turbulent wake flows behind two side-by-side cylinders. Journal of Fluids and Structures 18, 387–403.

Chen, S.S., 1986. A review of flow-induced vibration of two circular beams in crossflow. ASME Journal of Pressure Vessel Technology 108, 382–393.

Farge, M., 1992. Wavelet transforms and their applications to turbulence. Annual Review of Fluid Mechanics 24, 395–457.

Glowinski, R., Pironneau, O., 1992. Finite element methods for Navier–Stokes equations. Annual Review of Fluid Mechanics 24, 167–204.

Guillaume, D.W., LaRue, J.C., 1999. Investigation of the flopping regime with two-, three-, and four-cylinder arrays. Experiments in Fluids 27, 145–156.

Guillaume, D.W., LaRue, J.C., 2003. Investigation of peak frequencies in the flopping regime with a two-cylinder array. Journal of Fluids and Structures 17, 331–335.

Ichioka, T., Kawata, Y., Nakamura, T., Izumi, H., Kobayashi, T., Takamatsu, H., 1997. Research on fluid elastic vibration of beam arrays by computational fluid dynamics (analysis of two beams and a beam row). JSME International Journal Series B 40, 16–24.

Jester, W., Kallinderis, Y., 2003. Numerical study of incompressible flow about fixed cylinder pairs. Journal of Fluids and Structures 17, 561–577.

Kim, H.J., Durbin, P.A., 1988. Investigation of the flow between a pair of circular beams in the flopping regime. Journal of Fluid Mechanics 196, 431–448.

Liu, Y., So, R.M.C., Lau, Y.L., Zhou, Y., 2001. Numerical studies of two side-by-side elastic cylinders in a cross flow. Journal of Fluids and Structures 15, 1009–1030.

Meneghini, J.R., Sahara, F., Siqueira, C.L.R., Ferrari Jr., J.A., 2001. Numerical simulation of flow interference between two circular cylinders in tandem and side-by-side arrangements. Journal of Fluids and Structures 15, 327–350.

Ng, C.W., Cheng, V.S.Y., Ko, N.W.M., 1997. Numerical study of vortex interactions behind two circular beams in bistable flow regime. Fluid Dynamics Research 19, 379–409.

Peschard, I., Le Gal, P., 1996. Coupled wakes of cylinders. Physical Review Letters 77, 3122–3125.

Slaouti, A., Stansby, P.K., 1992. Flow around two circular beams by the random-vortex method. Journal of Fluids and Structures 6, 641–670.

So, R.M.C., Liu, Y., Chan, S.T., Lam, K., 2001. Numerical studies of a freely vibrating cylinder in a cross flow. Journal of Fluids and Structures 15, 845–866.

So, R.M.C., Wang, X.Q., 2003. Vortex-induced vibrations of two side-by-side Euler–Bernoulli beams. Journal of Sound and Vibration 259, 677–700.

Stokes, N., Mooney, J., 1994. Manual for Fastflo (Unix version), Version 2, CSIRO, Australia.

Sumner, D., Price, S.J., Paidoussis, M.P., 1997. Investigation of impulsively-started flow around two side-by-side circular cylinders: application of particle image velocimetry. Journal of Fluids and Structures 11, 597–615.

Sumner, D., Price, S.J., Paidoussis, M.P., 1999. Fluid behavior of side-by-side circular cylinders in steady cross-flow. Journal of Fluids and Structures 13, 309–338.

Torrence, C., Combo, G.P., 1998. A practical guide to wavelet analysis. Bulletin of the American Meteorological Society 79, 61–78.

Wang, X.Q., So, R.M.C., Liu, Y., 2001. Flow-induced vibration of an Euler–Bernoulli beam. Journal of Sound and Vibration 243, 241–268.

Wardlaw, R.L., 1994. Interference and proximity effects. In: Sockel, H. (Ed.), Wind-excited Vibrations of Structures. Springer, Berlin.

Williamson, C.H.K., 1985. Evolution of a single wake behind a pair of bluff bodies. Journal of Fluid Mechanics 159, 1–18.

Xu, S.J., Zhou, Y., So, R.M.C., 2003. Reynolds number effects on the flow structure behind two side-by-side cylinders. Physics of Fluids 15, 1214–1219.

Zdravkovich, M.M., 2003. Flow Around Circular Cylinders. Oxford University Press, Oxford.